RSC Advances

PAPER

View Article Online
View Journal | View Issue

Cite this: *RSC Adv.*, 2022, **12**, 33142

Potent antibacterial activity of MXene–functionalized graphene nanocomposites

Mohammed Sadey Salmi,[a] Usman Ahmed,[a] Navid Aslfattahi,[d] Saidur Rahman,[b] John George Hardy [ce] and Ayaz Anwar [*a]

Received 8th August 2022
Accepted 11th October 2022

DOI: 10.1039/d2ra04944a

rsc.li/rsc-advances

Two dimensional (2D) nanomaterials display properties with significant biological utility (*e.g.*, antimicrobial activity). In this study, MXene–functionalized graphene (FG) nanocomposites with $Ti_3C_2T_x$ in varying ratios (FG : $Ti_3C_2T_x$, 25 : 75%, 50 : 50%, and 75 : 25%) were prepared and characterized *via* scanning electron microscopy, scanning electron microscopy-energy dispersive X-ray (SEM-EDX), high-resolution transmission electron microscopy (HRTEM), and zeta potential analysis. Their cytotoxicity was assessed using immortalized human keratinocytes (HaCaT) cells at three different timepoints, and antibacterial activity was assessed using Gram-positive Methicillin resistant *Staphylococcus aureus*, MRSA, and Gram-negative neuro-pathogenic *Escherichia coli* K1 (*E. coli* K1) *in vitro*. The nanomaterials and composites displayed potent antibacterial effects against both types of bacteria and low cytotoxicity against HaCaT cells at 200 μg mL^{-1}, which is promising for their utilization for biomedical applications.

Introduction

According to the world health organization (WHO), antibiotic resistance has become a prime threat to human life, and agriculture. The development of antibiotic resistance has provided a valid research motivation to find newer antibacterial agents, which will propagate antibacterial action whilst evading bacterial resistance.[1,2] Nanomaterials may display significant antibacterial action, and in comparison to antibiotics, nanomaterials have a much better chance of withstanding and evading bacterial resistance due to their good membrane permeability and bio-/cyto-compatibility.[3,4] Carbon nanotubes, metal and metal oxide nanomaterials, transition metal carbides such as $Ti_3C_2T_x$, and graphene derivatives have been reported to display significant bactericidal action.[5–8] Such nanomaterials can confer antibacterial effects through a variety of physical and chemical mechanisms (including direct physical contact, oxidative stress, photothermal ablation, photocatalytic activity; including multi-mode synergistic antibacterial effects), and for use in drug delivery, photodynamic therapy, and other medical applications.[9–15] Due to their high potency as antimicrobial agents, 2D nanomaterials have been deployed as antibacterial agents at lower doses than traditional antibiotics, which assists in overcoming antibacterial resistance, and other consequential side effects associated with biological use.[16–18] 2D graphene derivative-based nanomaterials and 2D nanomaterials beyond graphene have displayed significant promise in the fields of catalysis, optoelectronics, and biomedicine due to their desirable physicochemical properties and facile surface modification; having been reported to be highly potent antibacterial agents. Examples of such 2D nanomaterials include transition metal carbides and nitrides (MXenes), graphene derivatives, transition metal dichalcogenides (TMDCs), transition metal oxides (TMOs), graphitic carbon nitride (g-C_3N_4), black phosphorus (BP), layered double hydroxides (LDHs), *etc.*[2,13–15]

Graphene family nanomaterials (GFN) and MXenes are nanomaterials with very high antibacterial potential and MXenes have low toxicity towards human cells. For graphene-based nanomaterials, it is agreed upon that their cytotoxicity towards micro-organisms, animals, and human cells is dependent on a multitude of factors such as surface functional groups, charges, coatings, sizes and structural defects. Nanographene, with ultra-small sizes, biocompatible surface coatings, excellent dispersibility and stability in physiological environments, appears to be much less harmful *in vitro* to cells and *in vivo* to animals.[8,19–23] Furthermore, have been reported to be effective in anticancer therapy, biosensing and bioimaging, drug delivery, and photothermal therapy.[24–27] Both GFNs and $Ti_3C_2T_x$ MXenes have been reported to display physical and chemical mechanisms of antibacterial effects. For GFNs, the

[a]*Department of Biological Sciences, School of Medical and Life Sciences, Sunway University, Selangor, 47500, Malaysia. E-mail: ayazanwarkk@yahoo.com; Fax: +60-(0)3-5635-8630; Tel: +60-(0)3-7491-8622 ext. 7174*

[b]*Research Centre for Nano-Materials and Energy Technology, School of Engineering and Technology, Sunway University, Selangor, Malaysia*

[c]*Department of Chemistry, Faraday Building, Lancaster University, Lancaster, Lancashire, LA1 4YB, UK*

[d]*Department of Fluid Mechanics and Thermodynamics, Faculty of Mechanical Engineering, Czech Technical University in Prague, Technická 4, 166 07 Prague, Czech Republic*

[e]*Materials Science Institute, Faraday Building, Lancaster University, Lancaster, Lancashire, LA1 4YB, UK*

physical antibacterial mechanisms were reported to be insertion/cutting of GFNs into cells, as well as extraction of phospholipids, and photothermal ablation, and wrapping mechanisms; the chemical mechanisms include charge transfer and oxidative stress.[26] For $Ti_3C_2T_x$ MXenes physical mechanisms include contact mediated adhesion which disrupts cell wall and cell membrane integrity and leads to leaking of intracellular contents; wrapping of MXene sheets around bacterial cells also occurs with the application increased concentration of MXenes, and chemical mechanisms induced by $Ti_3C_2T_x$ include reactions with some components of the cell wall and cell membrane which compromises their morphology, as well as generation of reactive oxygen species (ROS) to create oxidative stress, which damages bacterial cells.[6] A novel approach combining graphene derivatives and MXenes to form MXene-based nanocomposites. Functionalization of graphene derivatives with certain functional groups may make them hydrophilic, which is useful for many biomedical applications due to the high water content of biological systems.[28]

In this paper, we report the synthesis of $Ti_3C_2T_x$ MXene–FG derivatives, and the preparation of nanocomposites composed of 25% $Ti_3C_2T_x$–75% FG, 50% $Ti_3C_2T_x$–50% FG, and 75% $Ti_3C_2T_x$–25% FG. The systematic variations in the weight% of $Ti_3C_2T_x$ and FG derivatives enabled assessment of whether such variations impart tunable antibacterial and/or cytotoxic effects. The materials were characterized using zeta potential analysis, scanning electron microscopy (SEM), and high-resolution scanning electron microscopy (HRTEM). The bactericidal effects of such materials were assessed using Gram-positive MRSA and Gram-negative *E. coli* K1, and their interactions were mapped with scanning electron microscopy (SEM). The cytotoxicity of such materials was analyzed *via* the treatment of immortalized HaCaT cells, monitoring the release of lactate dehydrogenase (LDH), an indicator of cell membrane damage, from the cells. This paper builds upon previous research work where $Ti_3C_2T_x$ MXene, and pristine graphene were used to assess their antibacterial potential[6,7,29–31] and the novelty lies in the use of functionalized graphene derivatives, and systematic variations in composition of $Ti_3C_2T_x$–FG nanocomposites, enabling determination of whether the nanocomposites provide improved antibacterial activity and lower cytotoxicity than pristine $Ti_3C_2T_x$ and pristine graphene.

Materials

All chemicals, solvents, and reagents were purchased from Sigma-Aldrich (California, USA) unless stated otherwise.

Methods

Synthesis of $Ti_3C_2T_x$ MXene

30 mL of HCl (6 M) solution was prepared by mixing 15 mL of concentrated HCl with 15 mL of deionized (DI) water in a 50 mL beaker. 3 g of LiF was then added to the HCl solution, and this mixture stirred at 300 rpm for 30 minutes until the LiF was completely dissolved. The Ti_3AlC_2 MAX phase was then added to the etchant mixture slowly to prevent overheating in the exothermic reaction, and the resultant solution was stirred at 40 °C for 48 hours. This etching process was followed by addition of dilute solution of NaOH until the pH of the solution reached 6, after which the solution was filtered, and the solid product was rinsed several times with DI water. The product was washed a further four times by centrifugation (each interval of 10 min at 3500 rpm) using an ultrahigh speed centrifuge (Sorvall LYNX 6000, Thermo Scientific). The obtained multilayered Ti_3C_2 MXene was sonicated for 1 hour using an ultrasonic probe sonicator (FS-1200 N) in order to obtain delaminated singular Ti_3C_2 MXene flakes. The synthesized delaminated MXene flakes were then dried in a vacuum oven.[32]

Synthesis of functionalized graphene (FG)

Graphene was functionalized due to its hydrophobicity *via* acid treatment (treatment of GNP with 3 : 1 ratio of sulphuric and nitric acid) to introduce functional groups such as hydroxyl groups and carboxyl groups onto the surface of graphene nanoplatelet sheets, thereby making graphene nanoplatelets (GNP) compatible with polar solvents such as ultrapure water. 400 mg of GNPs was added slowly to H_2SO_4 (66 mL, 18.5 M). This was followed by stirring of the solution at a speed of 300 rpm at room temperature and pressure for 30 minutes. Then the beaker with the graphene suspension in H_2SO_4 was moved to an ice bath. Next 34 mL (12 M) of nitric acid (HNO_3) was added very slowly dropwise to the graphene in H_2SO_4 suspension, followed by stirring in ice covered conditions for 1 hour. The mixture was then allowed to stir for 24 hours at room temperature. After that, the mixture was sonicated at 64 kHz for a six-hour period with 30 seconds on, and 30 seconds off alternating periods, followed by stirring of the resultant acidified GNPs for 24 hours. The acidified GNPs were then stirred for 3 hours at room temperature. This was followed by thoroughly washing the acidified GNPs with distilled water and then centrifugation at 7000 rpm for 15 minutes at 24 °C. After the first centrifugation step, the product was treated with more distilled water and centrifuged again. Four rounds of washing and centrifugation were performed. These washing and centrifugation steps were performed to free the acidified GNP product of any residual acid. After removal of residual acid by washing and centrifugation, the product was incubated in a drying oven for 24 hours at 60 °C. The product after drying was ground with a pestle and mortar to yield powdered hydrophilic hydroxyl group and carboxyl group functionalized graphene.

Synthesis of $Ti_3C_2T_x$–FG nanocomposites

For preparation of each of nanocomposites of 50% $Ti_3C_2T_x$ MXene–50% FG, 75% $Ti_3C_2T_x$ MXene–25% FG, and 25% $Ti_3C_2T_x$ MXene–75% FG, the protocol was as follows:

To make 30 mg of the 50% FG 50% $Ti_3C_2T_x$, a pure colloid of FG was prepared by mixing 15 mg of FG in 40 mL of DI H_2O. After mixing, the solution was magnetically stirred under 60 °C and 600 rpm. After stirring, then the colloid was sonicated for one hour, with 5 seconds on and 3 seconds off with 60% amplitude. A pure colloid of $Ti_3C_2T_x$ was then prepared by mixing 15 mg of $Ti_3C_2T_x$ in 40 mL of DI H_2O. After mixing, the

solution was then transferred to the hot plate for magnetic stirring at 60 °C and 600 rpm. After stirring, then the colloid was sonicated for one hour, with 5 seconds on and 3 seconds off with 60% amplitude. After sonication of both the pure colloids, then the two colloids are mixed, followed by magnetic stirring at 60 °C and 600 rpm. After stirring, the colloid mixture was sonicated for one hour, with 5 seconds on and 3 seconds off with 60% amplitude. Filtration and centrifugation processes were utilized for the extraction of MXene and FG nanosheets, and for the formation of their colloids, whilst for the formation of the nanocomposite colloids, the principle lies in mixing the individual MXene and functionalized graphene colloids and properly stirring and sonication to result in a harmonized suspension.

For preparation of 30 mg of 75% $Ti_3C_2T_x$–25% FG, the pure colloid of $Ti_3C_2T_x$ was prepared by mixing 22.5 mg of $Ti_3C_2T_x$ in 40 mL of DI H_2O. The pure colloid of FG was prepared by mixing 7.5 mg of functionalized graphene in DI H_2O. The rest of the protocol is the same as aforementioned as the protocol of 50% $Ti_3C_2T_x$–50% FG. Filtration and centrifugation processes were utilized for the extraction of MXene and FG nanosheets, and for the formation of their colloids, whilst for the formation of the nanocomposite colloids, the principle lies in mixing the individual MXene and functionalized graphene colloids and properly stirring and sonication to result in a harmonized suspension.

For preparation of 30 mg of 25% $Ti_3C_2T_x$–75% FG, the pure colloid of $Ti_3C_2T_x$ was prepared by mixing 7.5 mg of $Ti_3C_2T_x$ in DI H_2O. The pure colloid of FG was prepared by mixing 22.5 mg of FG in DI H_2O. Regarding isolation of the composites, the pure MXene and functionalized graphene underwent filtration and centrifugation protocols, and these pure nanocolloids were mixed, stirred and sonicated to form harmonized suspension.

Scanning electron microscopy (SEM) and scanning electron microscopy-energy dispersive X-ray analysis (SEM-EDX)

Dispersity and homogeneity of the prepared nanofluids was assessed by scanning electron microscopy (VEGA 3, TESCAN) and elemental analysis was performed by energy dispersive spectroscopy (EDX, OXFORD INSTRUMENT). A digital ion coater (COXEM Co, SPT-20) was recruited to coat the samples with Pt at a fixed current of 3 mA for 300 s for SEM imaging.

Energy dispersive X-ray spectroscopy (EDX) was performed in order to determine the elemental profiles across regions of $Ti_3C_2T_x$, FG, 50% $Ti_3C_2T_x$–50% FG, 25% FG–75% $Ti_3C_2T_x$ and 75% FG–25% $Ti_3C_2T_x$.

Zeta potential analysis

The Litesizer 500 Anton Paar was used to determine the stability of the MXene, FG, 50% MXene–50% FG, 25% FG–75% MXene, 75% FG–25% MXene colloidal solutions. The principle of electrophoretic light scattering (ELS) is used to infer the stability of the colloidal solutions by the instrument. The Litesizer 500 had a controlled temperature within the range of 0–90 °C. The instrument was equipped with a light source of 40 mW power, and wavelength of 658 nm. The zeta potential measuring range is from −200 to +200 mV with a sensitivity of 1 mg mL^{-1} (lysozyme) and maximum sample concentration of 40% w/v.

High resolution transmission electron microscopy (HRTEM)

HRTEM was conducted in order to assess the lattice fringes of the colloidal samples, and the lattice fringes of the sample pertain to the atomic planes of the specimen. HRTEM was performed using HRTEM (JEOL JEM-ARM 200F) image using an accelerating voltage of 200 kV.

Bacteria and cell cultures

Clinical strains of methicillin-resistant *Staphylococcus aureus* (MRSA) (MTCC 381123), and neuropathogenic *Escherichia coli* (018:K1:H7) (MTCC 710859) were cultivated in nutrient broth and grown at 37 °C overnight on a shaker. HaCaT cells were cultured in T-75 cm^2 culture flask in complete medium (RPMI-1640 containing 10% FBS, 10% Nu-Serum, 2 mM glutamine, 1 mM pyruvate, penicillin (100 units per ml), streptomycin (100 μg per ml), non-essential amino acids and vitamins).[33]

Bactericidal assay

The antibacterial activity of $Ti_3C_2T_x$ MXene–FG nanocomposites was assessed *via* a bactericidal assay. In this assay, MRSA and *E. coli* K1 bacteria were adapted to their log phase by fixing them to an optical density of 0.22 at 595 nm using a spectrophotometer (OD_{595} = 0.22), whereby absorbance of 0.22 at 595 nm corresponds to 10^8 colony forming units per mL (CFU mL^{-1}) of bacteria. Various concentrations of the $Ti_3C_2T_x$ MXene–FG nanocomposite material colloid were then prepared and to these concentrations 10 μL of the aforementioned bacterial culture (equivalent to approximately 10^6 CFU mL^{-1}) was added in 1.5 mL centrifuge tubes followed by incubation at 37 °C for 2 hours. Negative control samples were prepared with bacteria + phosphate buffered saline (PBS), and positive control samples were prepared by incubating the bacteria with 100 μg mL^{-1} gentamicin. Following incubation at 37 °C for 2 hours, the bacteria treated with samples, negative controls, and positive controls were serially diluted in a 96 well plate and 10 μL of the dilutions were plated on nutrient agar plates. The agar plates were then incubated at 37 °C overnight, and then 24 hours later the viable bacterial CFU was counted.

SEM with bacteria

MRSA and *E. coli* K1 bacteria were treated with $Ti_3C_2T_x$, FG, 25% FG:75% $Ti_3C_2T_x$, 50% FG:50% $Ti_3C_2T_x$, 75% FG:25% $Ti_3C_2T_x$ colloidal solutions and then fixed on glass cover slips using glutaraldehyde. The fixed slides were then washed with ethanol and the images of possible bacteria-nanomaterial/nanocomposite interaction were then examined using a SEM (VEGA 3, TESCAN) instrument. Prior to the observations, the specimens were coated with a thin layer of gold (approximately 15 nm) with the use of sputter-coater (Quorum Q150T S).

Assessment of total ROS

In the present study, the total ROS produced was measured by using 2′,7′-dichlorodihydrofluorescein diacetate (DCFH-DA; Sigma Aldrich). Essentially, 1×10^8 CFU mL^{-1} bacterial cultures were treated with $Ti_3C_2T_x$ MXene, functionalized graphene, 75% $Ti_3C_2T_x$:25% functionalized graphene, 50% $Ti_3C_2T_x$:50% functionalized graphene and 25% $Ti_3C_2T_x$:75% functionalized graphene 2D nanomaterials at two different concentrations (100 and 200 μg mL^{-1}). After treatment, the cells were incubated for two hours at 37 °C in shaking incubator. Following incubation, the cells were washed with PBS twice and treated with serum free RPMI-1640 having 25 μg mL^{-1} DCFHDA followed by incubation at 37 °C for 45 minutes in dark. The non-fluorescent DCFHDA converted to DCF by intracellular esterases, which produce green fluorescence. The cells were then washed with PBS and the pellet was re-suspended in RPMI-1640. The cells were transferred to 96 well plate and the degree of DCF was measured by microplate reader. The fluorescence intensity was quantified at 485 nm excitation and 535 nm emission wavelength. The images of ROS were recorded by fluorescence microscopy at 200×.

Human keratinocyte cells culture and maintenance

Human keratinocytes skin cells (HaCaT) (RRID: CVCL_0038) procured from Cell Lines Services (CLS, Germany) were cultured and maintained in RPMI-1640 supplemented with 10% of each ingredient *i.e.*, penicillin (100 units per mL), streptomycin (100 μg mL^{-1}), foetal bovine serum (FBS), glutamine (2 mM), pyruvate (1 mM), vitamins and non-essential amino acids (NAA). The cells were cultured in 75 cm^2 culture flasks in CO_2 incubator. After 80% confluency, the old media was aspirated, and the monolayer was detached by adding 2 mL trypsin. The suspension was than centrifuged at 2500 rpm for 5 minutes at room temperature. The pellet was re-suspended and seeded in 96 well plate. The plates were incubated in a standard 5% CO_2 incubator at 37 °C for 24 hours until the uniform monolayer was observed under microscope.

Cytotoxicity analysis

This assay assesses the release of lactate dehydrogenase (LDH) from cells, whereby LDH release from cells indicates that the cell membrane has ruptured. Greater LDH release indicates greater cell membrane rupture.[34] For this assay, HaCaT cells were used to assess cytotoxicity. Keratinocytes should be the most appropriate target cells for assessing the sensitivity of the skin to toxicants.[35] Cytotoxicity assay has been performed to assess whether any cytotoxicity is imparted from $Ti_3C_2T_x$ MXene–FG nanocomposites to the HaCaT cells. The same concentrations of $Ti_3C_2T_x$ MXene–FG nanocomposites were treated with a uniform monolayer of HaCaT cells in a 96 well plate. This treatment was followed by incubation of the respective treated cells for 12, 24, and 48 hours at 37 °C in a 5% CO_2 incubator. The incubation period was followed by collection of supernatants from each of the wells and then the cytotoxicity was determined by quantifying the release of LDH from the cells using an LDH kit (Invitrogen). Cells not treated with any of the nanocomposite samples were considered as negative controls, and cells treated with 0.1% Triton-X100 were considered to be positive control, as Triton-X100 instigates cell lysis and causes maximum LDH release from cells. The percentage cell cytotoxicity was calculated by the formula % cytotoxicity = ((sample absorbance − negative control absorbance)/(positive control absorbance − negative control absorbance) × 100).

Results

SEM-EDX

$Ti_3C_2T_x$ MXene. The morphology of the pure $Ti_3C_2T_x$ MXene nanomaterial was studied *via* SEM (Fig. 1A). The formation of self-stacking $Ti_3C_2T_x$ MXene multilayers in an accordions like arrangement is evident, which corroborates previous findings.[36–38] This accordion like multilayered structure emerges when Al atoms are etched out from between Ti_3AlC_2 layers with the acid treatment of multilayered Ti_3AlC_2 MAX Phase. This etching leaves the multilayered $Ti_3C_2T_x$ where van der Waals bonds between the individual layers hold the layers together.[37] Elemental analysis of $Ti_3C_2T_x$ was assessed at 3 sites with EDX (Table 1), and the ratio of Ti and C was observed to be: Ti mean atomic% was 42.67 ± 7.97%, and C mean atomic% was 57.33 ± 7.97%.

Functionalized graphene. The morphology of the FG is displayed in Fig. 1B, a single layer arrangement is seen whereby the insertion points represent functional groups that have been attached onto the pristine graphene 2D nanosheets. Elemental analysis of FG was assessed at 2 sites with EDX (Table 1), and the ratio of C and O was observed to be: C mean atomic% was 91.04 ± 1.58% and O mean atomic% was 8.97 ± 1.58%.

25% $Ti_3C_2T_x$:75% functionalized graphene. The morphology of the 25% FG:75%$Ti_3C_2T_x$ is shown in Fig. 1C which shows a saturation of multilayered accordions like $Ti_3C_2T_x$ sheets, and very few single layers FG nanosheets, which are intercalated between Ml–MXenes. Elemental analysis of 25% FG:75% $Ti_3C_2T_x$ was performed across 4 sites (Table 1), and presence of C, O and Ti was observed to be: C atomic% was 85.75 ± 7.00%, O atomic% was 11.9 ± 4.61%, and Ti atomic% was 2.35 ± 2.53%.

50% FG:50% $Ti_3C_2T_x$. The morphology of the 50% FG:50% $Ti_3C_2T_x$ is shown in Fig. 1D. The presence of equal amounts of $Ti_3C_2T_x$ sheets, and FG sheets results in homogeneity of embedding of single layered FG nanosheets between layers of Ml–$Ti_3C_2T_x$ nanosheets. Elemental analysis was performed across 4 sites (Table 1), and presence of C, O, and Ti was observed to be: C atomic% was 81.82 ± 7.04%, O atomic% was 14.79 ± 4.86%, and the Ti atomic% was 3.39 ± 2.47%.

75% $Ti_3C_2T_x$:25% functionalized graphene. The morphology of 75% FG:25% $Ti_3C_2T_x$ is shown in Fig. 1E. The high saturation of single layered FG sheets was intercalated within the layers of finely dispersed multilayered-$Ti_3C_2T_x$ layers. Elemental analysis was performed across 5 sites (Table 1), and the atomic% of C was 53.88 ± 6.28%, O atomic% was 31.32 ± 3.93%, and Ti atomic% was 14.80 ± 2.82%.

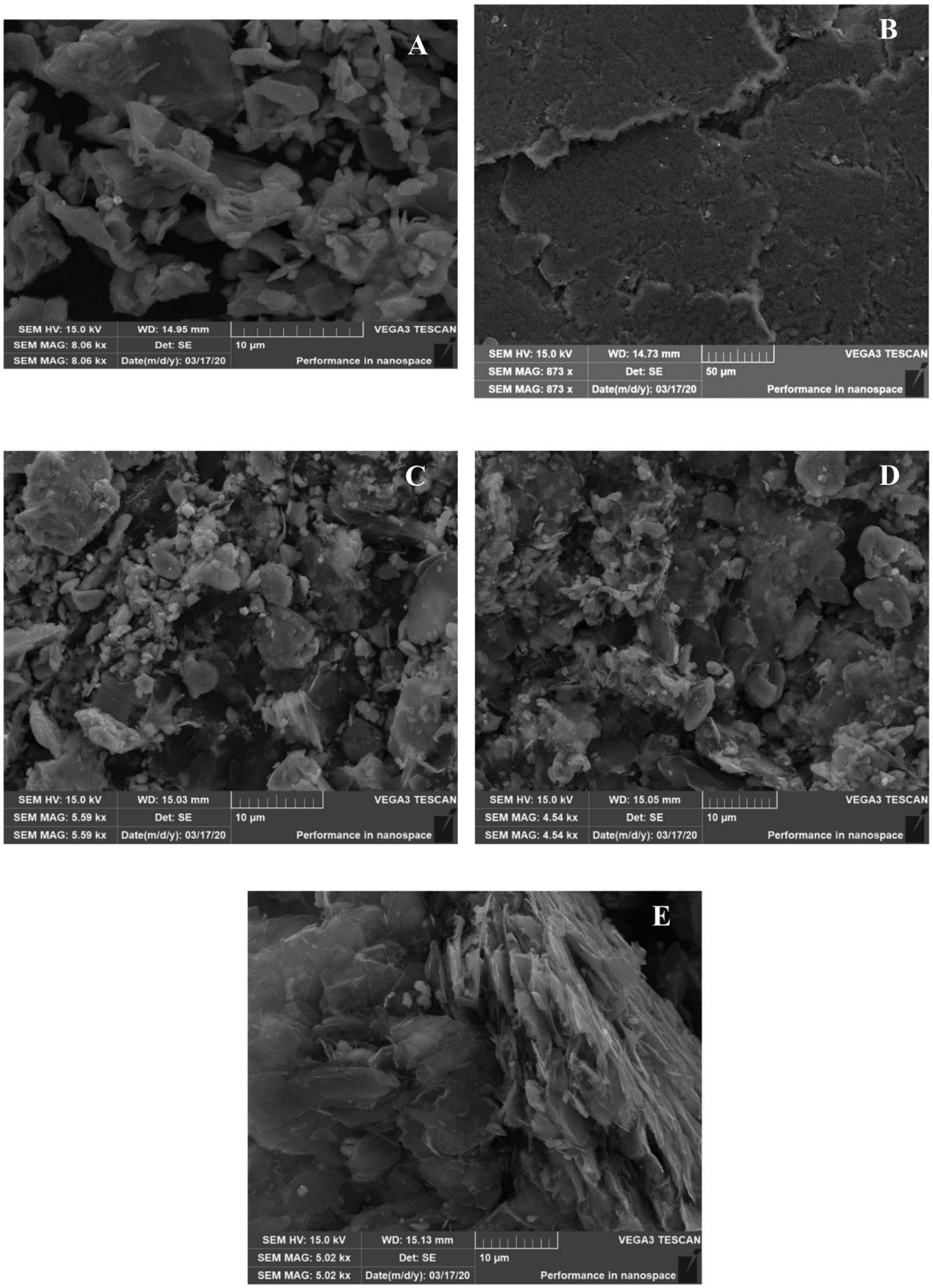

Fig. 1 (A) SEM image of colloidal $Ti_3C_2T_x$ nanosheets. (B) SEM Image of colloidal functionalized graphene nanosheets. (C) SEM image of colloidal 25% FG:75% $Ti_3C_2T_x$ nanosheets. (D) SEM image of colloidal 50% FG:50% $Ti_3C_2T_x$ nanosheets. (E) SEM image of colloidal 75% FG:25% $Ti_3C_2T_x$ nanosheets.

Zeta potential analysis

Zeta potential analysis offers insight into the physical stability of nanomaterial colloidal solutions.[39] Zeta potential is a measure of the potential difference between any point of the continuous base fluid of the colloidal solution and the point of attachment of a nanoparticle dispersed in the solvent used for the colloidal solution, and electrophoretic light scattering (ELS) and electroacoustic determination can measure zeta potentials.[40] A highly positive or highly negative zeta potential implies that the repulsive forces between the strongly charged dispersed

Table 1 Energy dispersive spectroscopy mean data

	$Ti_3C_2T_x$	75% $Ti_3C_2T_x$:25% f unctionalized graphene	50% $Ti_3C_2T_x$:50% functionalized graphene	25% $Ti_3C_2T_x$:75% functionalized graphene	Functionalized graphene
Titanium	42.67%	14.80%	3.39%	2.36%	
Carbon	57.33%	53.88%	81.82%	85.75%	91.04%
Oxygen		31.32%	14.79%	11.9%	8.97%

Table 2 Zeta potential of 2D nanomaterials and nanocomposites

2D nanomaterial/nanocomposite	Zeta potential (mV)
Functionalized graphene	−20.6
$Ti_3C_2T_x$ MXenes	−12.3
25% FG/75% $Ti_3C_2T_x$	−2.3
50% FG/50% $Ti_3C_2T_x$	−4.1
75% FG/25% $Ti_3C_2T_x$	−8.3

nanoparticles and particles of the base fluid dominate over any existing attractive forces, and this results in dispersion stability. In contrast, low negative or positive zeta potentials would indicate that the attractive forces between charged dispersed nanoparticles and particles of the base fluid would dominate over repulsive forces, and this would lead to aggregation, agglomeration, or flocculation of nanomaterials in the colloidal solutions.[41]

From Table 2, it can be deduced that FG is the most physically stable colloidal solution, as it has the most negative zeta potential of −20.6 mV. $Ti_3C_2T_x$ MXene has a zeta potential of −12.3 mV. Both $Ti_3C_2T_x$ MXene and FG possess surface negative charges due to the presence of negative functional groups on their surface layers. The combination of these 2D nanomaterials to form $Ti_3C_2T_x$–FG nanocomposites is expected to yield stable colloids, emanating from dominance of repulsive forces between $Ti_3C_2T_x$ and FG intercalated between $Ti_3C_2T_x$ multilayers. Furthermore, this repulsion is expected to increase with increasing FG composition in the nanocomposites, and this is observed in the data displayed in Table 2, where a 75% FG composition results in the zeta potential being −8.3 mV, a 50% FG composition resulting in zeta potential being −4.1 mV, and a 25% FG composition yielding zeta potential of −2.3 mV. This reaffirms that the order of colloidal solution stability is that 75% FG:25% $Ti_3C_2T_x$ > 50% FG:50% $Ti_3C_2T_x$ > 25% FG:75% $Ti_3C_2T_x$. FG provides more negatively charged species in the colloidal solutions and this leads to greater prevalence of repulsive forces in the colloidal solutions, contributing to more negative zeta potentials, thereby greater physical stability.

HRTEM

Fig. 2A displays $Ti_3C_2T_x$ nanosheets, notably flaky edges with evidence of stacking of a few layers of flakes. The presence of 2D flakes which are stacked and layered indicate this is MXene in line with the literature.[38,42–44] Fig. 2B shows completely transparent FG sheets that are stuck together, at the edges, the flakes are single layered, and at thicker areas a few layers of flakes are stuck together; in some areas the flakes appear to be crumpled due to the high surface area compared to the thickness, and literature suggests that wrinkling and folded edge features occur due to the functionalization procedure and acid treatment.[45–47] Fig. 2C displays the regular layered structure of the nanocomposite comprised of 25% FG:75% $Ti_3C_2T_x$. The long flakes in the middle are FG sheets, whilst the edges or light crystals are MXenes. In this sample, the lateral size of the graphene sheets is bigger than MXene, and MXene content is higher in terms of percentage. The FG sheets are stuck together while the MXene flakes are dispersed. MXene flakes are shown as crystalline whilst FG flakes appear to be crumpled. This finding corroborates previous literature.[3] Fig. 2D shows the nanocomposite comprised of 50% FG and 50% $Ti_3C_2T_x$ MXene. The blackish crystalline MXene flakes are scattered evenly throughout the composite with transparent FG sheets. Fig. 2E shows the 75% FG:25% $Ti_3C_2T_x$ MXene composite. The transparent bigger sheets are FG, and the crystallized parts are MXene (top right and bottom right parts and some scattered parts). This morphology can be ascribed to the fact that MXene flakes are scattered, and their lateral size is smaller and percentage content is lesser, whilst FG flakes are transparent and bigger in size, and also greater in terms of percentage content, and thus FG sheets show prominence over $Ti_3C_2T_x$ MXenes in this nanocomposite structure.

Bactericidal activity

High bactericidal activity was witnessed with the application of these nanomaterials, and nanocomposites on both MRSA and *E. coli* K1. In the bactericidal assay performed on MRSA (Fig. 3A), the best performing materials were 100 μg mL^{-1}, and 200 μg mL^{-1} of 75% FG–25% $Ti_3C_2T_x$, 50% FG–50% $Ti_3C_2T_x$, and FG, followed by pure $Ti_3C_2T_x$ and pure 25% FG–75% $Ti_3C_2T_x$ in that respective order. 75% FG–25% $Ti_3C_2T_x$, 50% FG–50% $Ti_3C_2T_x$, and FG showed bactericidal activity where no surviving colonies were observed after 2 hours of incubation of MRSA with these materials. On the other hand, FG–75% $Ti_3C_2T_x$ and pure $Ti_3C_2T_x$ also showed significant bactericidal activity, but some colonies of MRSA did survive. 200 μg mL^{-1} of $Ti_3C_2T_x$ displayed full bactericidal activity.

Application of these materials on *E. coli* K1 also produced significant bactericidal effect, albeit of a lower magnitude when the materials are used to treat Gram negative *E. coli* K1, as opposed to Gram positive MRSA bacteria, which is more vulnerable to the action of 2D nanomaterials.[48] 200 μg mL^{-1} of 75% FG–25% $Ti_3C_2T_x$, and 50% FG–50% $Ti_3C_2T_x$ showed

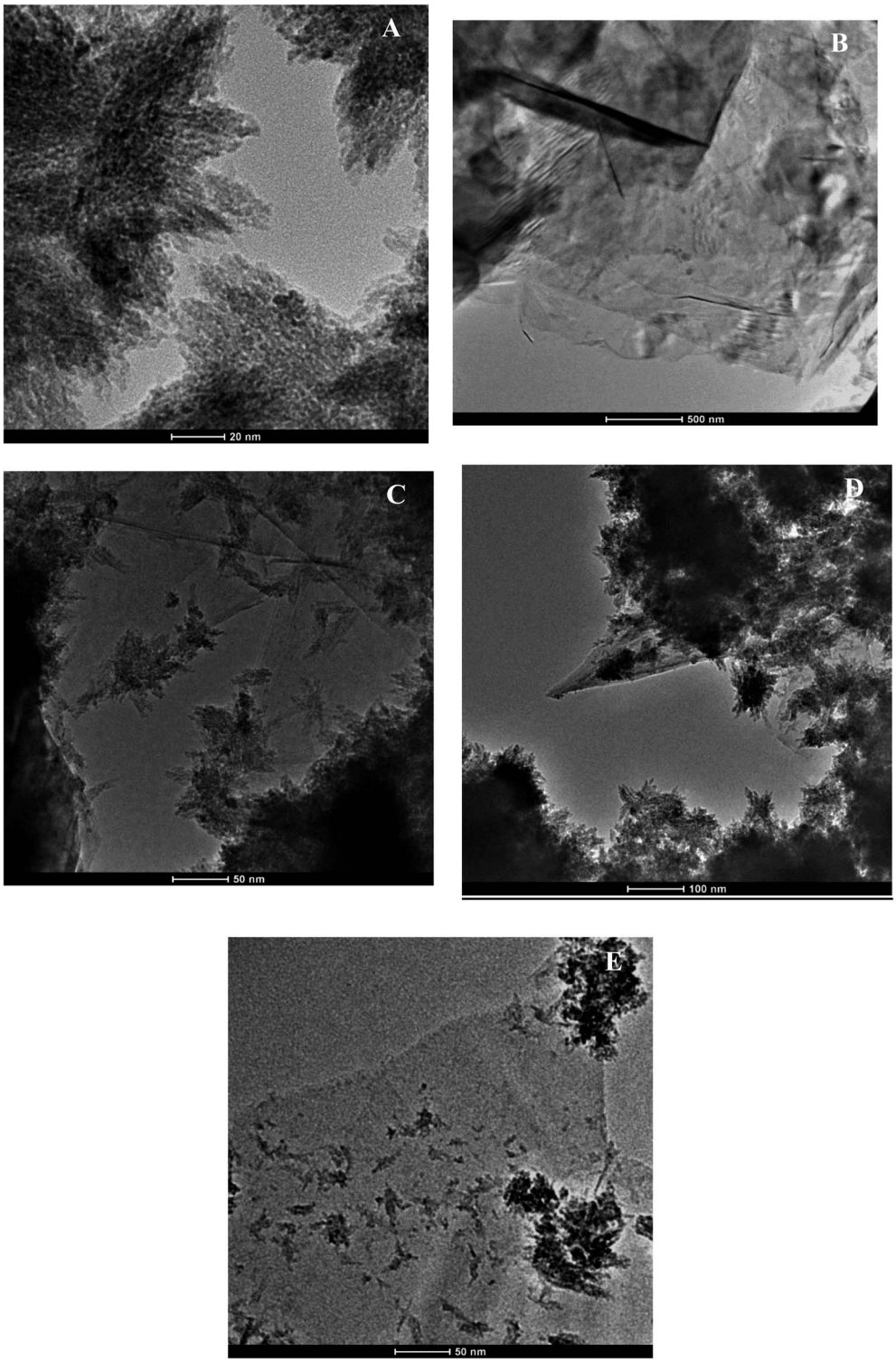

Fig. 2 (A) HRTEM image of $Ti_3C_2T_x$ MXene. (B) HRTEM image of functionalized graphene. (C) HRTEM image of 25% FG:75% $Ti_3C_2T_x$. (D) HRTEM image of 50% FG:50% $Ti_3C_2T_x$. (E) HRTEM image of 75% FG:25% $Ti_3C_2T_x$.

complete diminishing of *E. coli* K1 populations (Fig. 3B). Treatment of *E. coli* K1 with the materials also showed that 200 μg mL^{-1} of 75% FG–25% $Ti_3C_2T_x$ and 50% FG–50% $Ti_3C_2T_x$, killed *E. coli* K1 to the highest level, followed by 100 μg mL^{-1} of 75% FG–25% $Ti_3C_2T_x$ and 50% FG–50%. Thus, for anti *E. coli* K1 effect, the most effective materials are 75% FG–25% $Ti_3C_2T_x$, 50% FG–50% $Ti_3C_2T_x$, and FG, followed by 25% FG–75% $Ti_3C_2T_x$ and pure $Ti_3C_2T_x$.

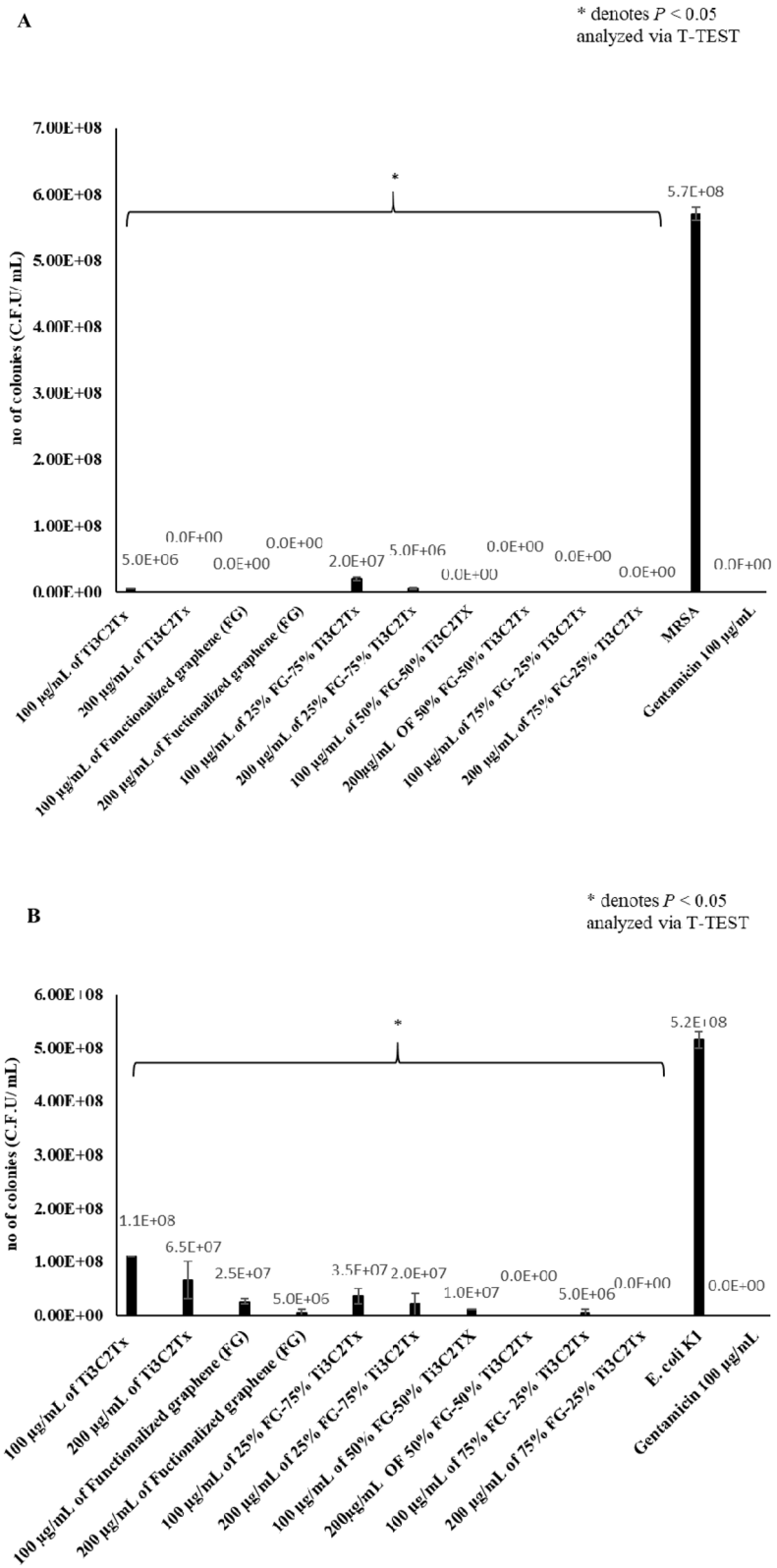

Fig. 3 (A) Bactericidal assay performed on MRSA using 100 µg mL^{-1} and 200 µg mL^{-1} concentrations of colloidal $Ti_3C_2T_x$ MXene, functionalized graphene, 25% FG:75% $Ti_3C_2T_x$, 50% $Ti_3C_2T_x$:50% FG, and 75% FG:25% $Ti_3C_2T_x$. (B) Bactericidal assay performed on *E. coli* K1 using 100 µg mL^{-1} and 200 µg mL^{-1} concentrations of colloidal $Ti_3C_2T_x$ MXene, functionalized graphene, 25% FG:75% $Ti_3C_2T_x$, 50% $Ti_3C_2T_x$:50% FG, and 75% FG:25% $Ti_3C_2T_x$. *Represents $p < 0.05$, obtained using *t*-test with two-tailed distribution.

SEM analysis

SEM was performed with the incorporation of bacterial cultures with 2D nanomaterial colloidal solutions, and the results show the interaction of synthesized 2D nanomaterials with both MRSA and *E. coli* K1. Fig. 4I delineates the interaction of pure $Ti_3C_2T_x$ MXene with MRSA bacteria. Fig. 4II shows the interaction of functionalized graphene sheets with single MRSA cells, and it can also be seen that the single flakes of the FG sheets come in direct contact with MRSA cells. Fig. 4IV and V also show the direct localization and "wrapping" of MRSA bacterial cells by 50% $Ti_3C_2T_x$–50% FG and 25% $Ti_3C_2T_x$–75% FG nanocomposites. Fig. 4VI shows untreated MRSA bacterial cells as negative control. Fig. 4VII shows several lysed *E. coli* cells with pure accordions like MXene sheets prevailing in the picture. This leads to the understanding that the *E. coli* cells have experienced a compromise of their cell membrane integrity after having interacted with the 2D MXene sheets. Fig. 4VIII also shows a compromise of *E. coli* cellular integrity upon interaction with functionalized graphene. Similar instances can be seen in pictures Fig. 4XI, X, and IX whereby direct interaction of *E. coli* cells with 75% $Ti_3C_2T_x$–25% FG, 50% $Ti_3C_2T_x$–50% FG and 25% $Ti_3C_2T_x$–75% FG can be seen.

Assessment of total ROS

This assay was performed to describe the extent of oxidative stress conferred by our 2D nanomaterials and 2D nanomaterial-based nanocomposites to MRSA and *E. coli* K1. Fig. 5A shows that upon application of 100 μg mL^{-1} of each material, a high oxidative stress in bacteria was observed as a means of chemical destruction mechanism. This ROS generation is highest for pure $Ti_3C_2T_x$, followed by 75% $Ti_3C_2T_x$–25% FG, 50% $Ti_3C_2T_x$–50% FG, 25% $Ti_3C_2T_x$–75% FG, and then functionalized graphene respectively against both bacteria.

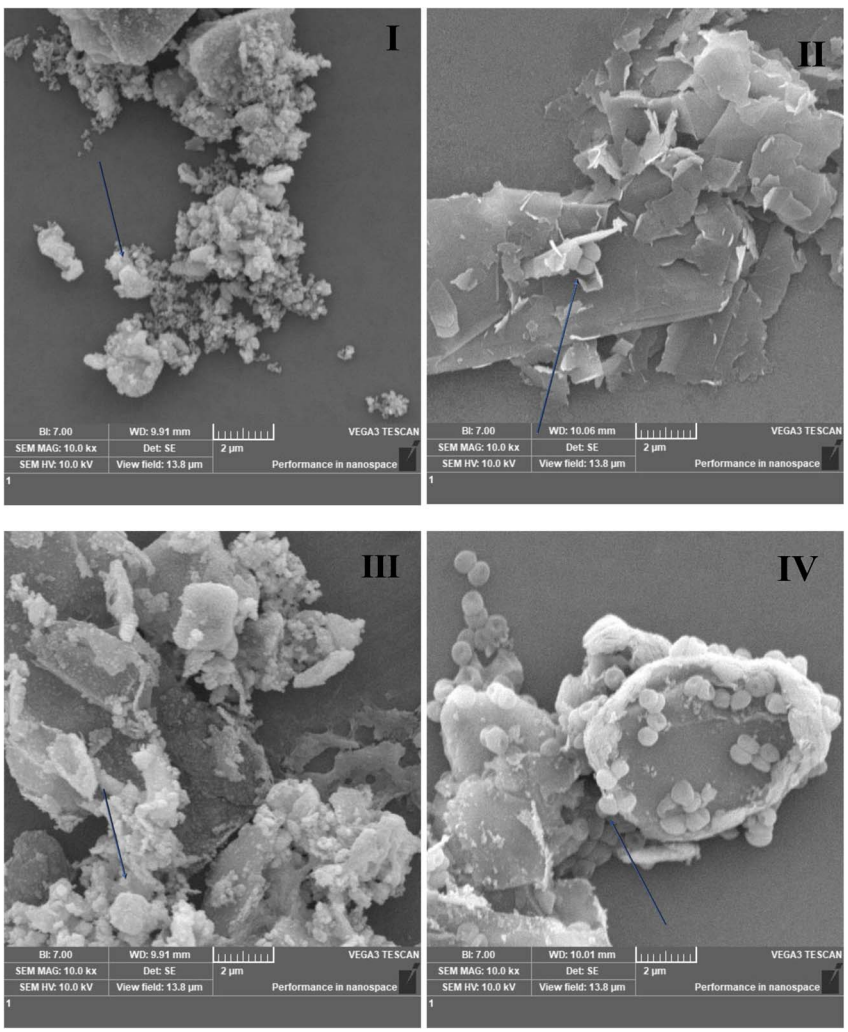

Fig. 4 SEM analysis. (I) 100 μg mL^{-1} $Ti_3C_2T_x$ with MRSA (II) 100 μg mL^{-1} FG with MRSA (III) 100 μg mL^{-1} 25% FG:75% $Ti_3C_2T_x$ with MRSA (IV) 100 μg mL^{-1} 50% FG:50% $Ti_3C_2T_x$ with MRSA (V) 100 μg mL^{-1} 75% FG:25% $Ti_3C_2T_x$ with MRSA (VI) MRSA (VII) 100 μg mL^{-1} $Ti_3C_2T_x$ with *E. coli* K1 (VIII) 100 μg mL^{-1} FG with *E. coli* K1 (IX) 100 μg mL^{-1} 25% FG: 75% $Ti_3C_2T_x$ with *E. coli* K1 (X) 100 μg mL^{-1} 50% FG:50% $Ti_3C_2T_x$ with *E. coli* K1 (XI) 100 μg mL^{-1} 75% FG:25% $Ti_3C_2T_x$ with *E. coli* K1 (XII) *E. coli* K1. Blue arrows denote areas where bacterial interaction with 2D nanomaterial frameworks occur.

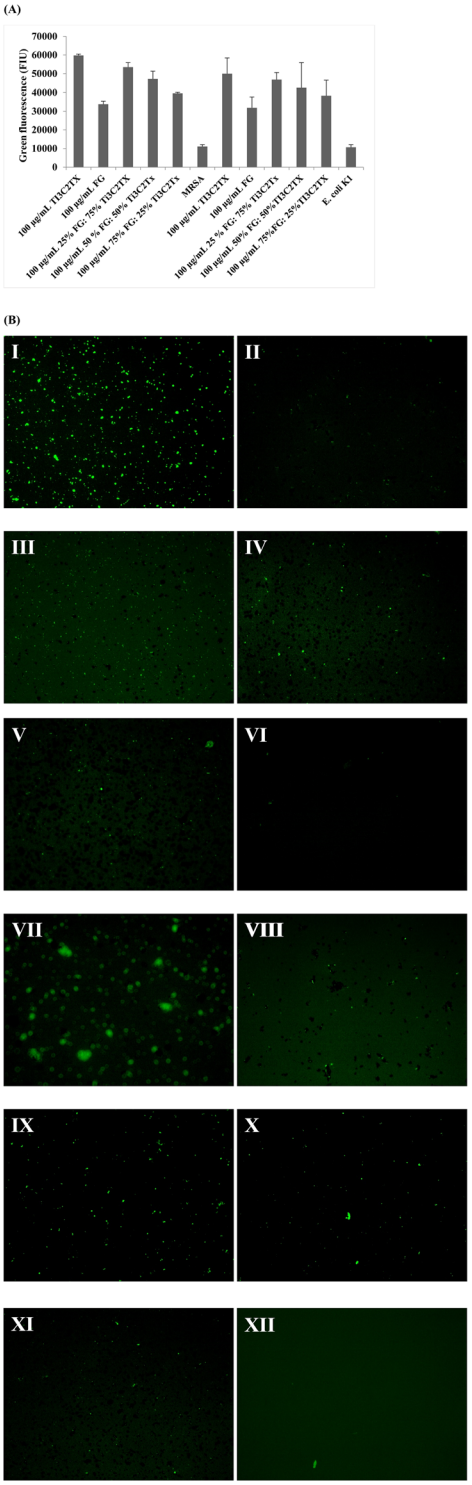

Fig. 5 (A) Reactive oxidative species (ROS) assessment of MRSA and *E. coli* K1 with nanomaterials and composites. (B) Fluorescent microscopy assessing the extent of oxidative stress of (I) 100 µg mL^{-1} $Ti_3C_2T_x$ with MRSA (II) 100 µg mL^{-1} FG with MRSA (III) 100 µg mL^{-1} 25% FG:75% $Ti_3C_2T_x$ with MRSA (IV) 100 µg mL^{-1} 50% FG:50% $Ti_3C_2T_x$ with MRSA (V) 100 µg mL^{-1} 75% FG:25% $Ti_3C_2T_x$ with MRSA (VI) MRSA (VII) 100 µg mL^{-1} $Ti_3C_2T_x$ with *E. coli* K1 (VIII) 100 µg mL^{-1} FG with *E. coli* K1 (IX) 100 µg mL^{-1} 25% FG:75% $Ti_3C_2T_x$ with *E. coli* K1 (X) 100 µg mL^{-1} 50% FG:50% $Ti_3C_2T_x$ with *E. coli* K1 (XI) 100 µg mL^{-1} 75% FG:25% $Ti_3C_2T_x$ with *E. coli* K1 (XII) *E. coli* K1. All images were captured at 200× magnification.

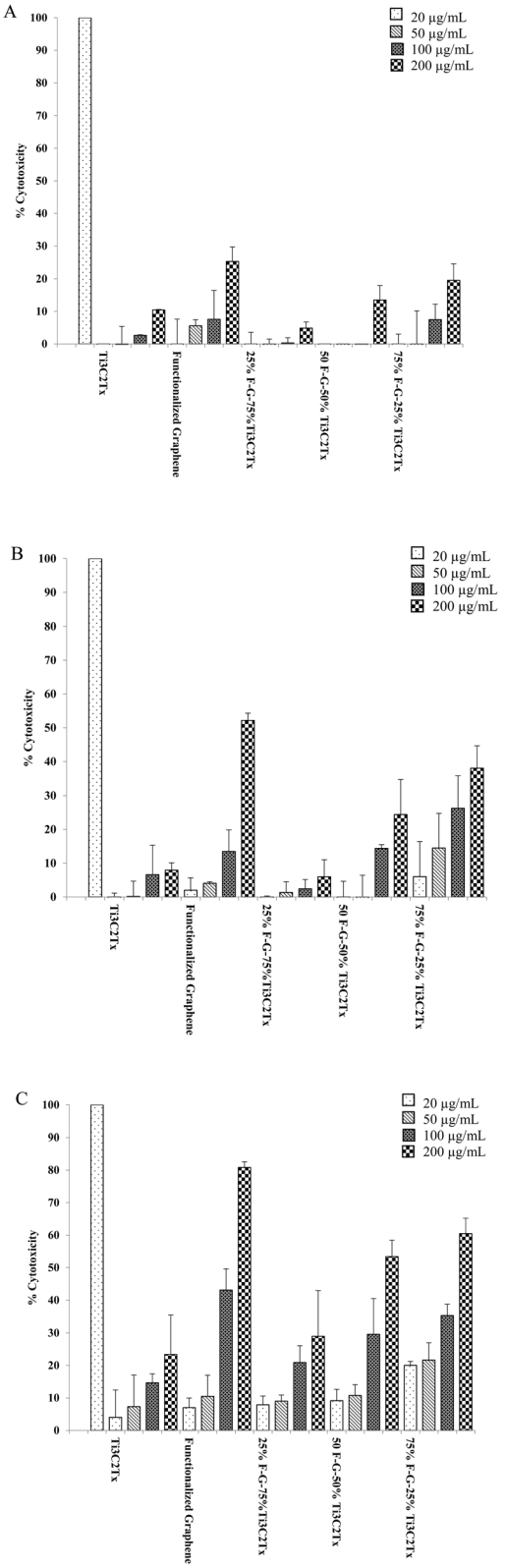

Fig. 6 Time dependent cytotoxicity analysis of HaCaT cells with nanomaterials and composites after (A) 12 hours, (B) 24 hours, and (C) 48 hours.

Fluorescence microscopy

Our fluorescence microscopy results (Fig. 5B) show a direct correlation to the ROS assessment whereby $Ti_3C_2T_x$ MXene treated bacteria showed highest manifestation of oxidative stress, followed by 75% $Ti_3C_2T_x$ MXene:25% FG, 50% $Ti_3C_2T_x$ MXene:50% FG, and 75% FG:25% $Ti_3C_2T_x$ MXene, and finally pure FG which conveyed the lowest manifestation of oxidative stress. This leads us to infer that regarding chemical destruction mechanisms, pure $Ti_3C_2T_x$ MXene is most active in generating ROS within bacteria and thus, this leads to greater relaying of chemical means of destroying bacterial cellular frameworks.

Time-dependent cytotoxicity assay

To show the effect of time of exposition of materials to human cell lines, time dependent cytotoxicity assay was performed after 12, 24, and 48 hours. The obtained results (Fig. 6) showed a trend whereby the cytotoxicity in human cells increases with time of exposition of cells to our 2D nanomaterials samples. Only pure functionalized graphene shows some noteworthy cytotoxic activity after 24 hours at high concentration of 200 μg mL^{-1}, however after 48 hours, the cytotoxicity of functionalized graphene and 50% $Ti_3C_2T_x$–50% FG and 25% $Ti_3C_2T_x$–75% FG increase to 80%, 55% and 60% respectively.

Discussion

2D nanomaterials have exceptional specific surface area that makes them large reservoirs as well as anchoring sites for effective loading and delivery of therapeutic agents.[50] This can also play into 2D nanomaterials possessing greater number of edge sites and contact sites which increases their chances of coming into contact with microbes for antimicrobial purposes. It can also make 2D nanomaterials more privy to functionalization for the tuning of their properties. Their high surface area to volume ratio also makes them amenable to stimuli such as light thus giving them local surface plasmon resonance (LSPR) effect in near infrared region (NIR 1 & 2) biowindows, thus making them agents for photothermal therapy. Due to their mechanical strength, and low toxicity, 2D nanomaterials also hold potential for tissue engineering applications.[50]

The prominence of graphene as a research interest spawned new classes of functional 2D nanomaterials such as transition metal dichalcogenides (TMDs), transition metal carbides, nitrides, and carbonitrides (MXenes), phosphorene, black phosphorus, layered double hydroxides, hexagonal boron nitride, metal organic frameworks *etc.* Since then, 2D nanostructure materials have been majorly deployed in bioelectronics, imaging, drug delivery, tissue engineering, and regenerative medicine, due to their exotic physicochemical properties, biocompatibility, biodegradability, surface functionality, and plasticity compared to their bulk precursors.[50]

Since 2011, after their discovery by Gogotsi *et al.*,[51] MXenes have garnered traction as a 2D nanomaterial for a multitude of applications. MXenes hold the innate advantages that are present in 2D nanomaterials such as outstanding mechanical, chemical, and physicochemical properties. Prospectively, MXenes possess two particular traits which make them attractive propositions for biomedical applications. Firstly, MXenes possess an array of surface terminations (such as oxygen, fluorine, hydroxyl groups *etc.*) which propagates their utility for drug loading, as well as loading of functional nanoparticles for hybrid formation, and hydrophilic biomacromolecules for surface modulation and all these possibilities allow MXenes to be tuned for further biomedical applications. Secondly, it has been widely reported that MXenes possess significant cytocompatibility which makes them especially relevant for biomedical applications. Due to the special structural, functional, and biological characteristics of MXenes and graphene such as superior electrical conductivity, high biocompatibility, large surface area, optical and magnetic features, and extraordinary magnetic and thermal properties, it is only rational to hold the viewpoint that nanocomposites of MXene–graphene would be able to fill voids in medical and biomedical engineering. Interestingly, machine learning can also be deployed to study the properties of MXene–graphene nanocomposites. Machine learning has already been used to model the physical properties of carbon nanotubes as well as predict the physical responses of carbon nanotubes for biomedical problems. Thus, these approaches can also be used to predict vibratory dynamics of MXene–graphene nanocomposites, as well as generate simulated or predicted physical responses of these nanocomposites for certain biomedical problems.[52] Machine learning can also be utilized in the area of new antibacterial drug design, and target identification. *In silico* identification of bacterial resistance mechanisms, and genes can be integrated with medicinal chemistry and nanomaterials science, so that MXene–graphene 2D nanocomposites can be made even more specific to be tailored to disrupt a particular bacterial serovar, or serotypes.[53]

The rationale of this study was literature precedent showing superior antibacterial activity of 2D nanomaterials and to explore opportunities for further optimization. 2D nanomaterials have ultrathin thickness, (normally) low toxicity (subject to synthetic methodology/purity/*etc.*), controllable size, and large surface area with unique physicochemical properties for easy surface modification and high photothermal efficiencies (as high as 100% in case of titanium carbide),[49] and can be chemically modified to tune their properties.[54–56] 2D nanohybrids and nanocomposites can provide supplemental/reinforced effects based on the properties of the different nanomaterials. Notably 2D nanomaterials for photothermal therapy (PTT) have demonstrated prolonged blood circulation, and high accumulation in tumors[55,56] performed a study where they synthesized expanded Ti_2C and Ti_3C_2 MXene phases from parent Ti_2AlC and Ti_3AlC_2 MAX phases under the same conditions using an aluminium extraction method to study differences in their biological activities (since Ti_2C and Ti_3C_2 share the same chemical composition and were synthesized from MAX phases with same chemical compositions under the same reaction conditions, any observed differences in biological activity would be due to differences in physical structure).[56] SEM analysis suggested that the expanded Ti_2C and Ti_3C_2 sheets

formed a network of slit-shaped nanopores, X-ray photoelectron microscopy for chemical analysis (ESCA-XPS) displayed no discrepancy in surface chemistry between Ti_2C and Ti_3C_2 MXenes; however, TEM results showed differences in atomic structure of the individual Ti_2C and Ti_3C_2 sheets. The distance between Ti–C layers in Ti_2C was measured to be 9.76 Å, which was 0.53 angstroms greater than the distance between Ti–C layers in Ti_3C_2 (9.23 Å). The antibacterial effect of the Ti_2C and Ti_3C_2 agents against *E. coli* K1 was studied, observing that Ti_2C had no antibacterial activity, whereas Ti_3C_2 displayed antibacterial activity, suggesting that the difference in stoichiometry between Ti_2C and Ti_3C_2 imparts subtle differences of physical structure at the atomic scale, and this determines differences in bioactivity of Ti_2C and Ti_3C_2 MXenes, despite their similarity in chemical composition.[30]

The antibacterial activity of graphene and graphene derivatives strongly depends on the accessible area, *i.e.*, edges and basal plane of sheets and structure of their agglomerates.[30] The surface functionality of graphene is one of the prime factors which determines the interaction of graphene with biological systems and microbes.[57–59] The functionality, chemical structure, and physicochemical properties of graphene can be modulated by means of covalent functionalization.[9,57] Graphene-based 2D materials with defined surface structure can be synthesized by mediating functionalization parameters in terms of number, position, and types of functional groups.[60] Graphene 2D materials with zwitterionic 2D surfaces can be produced by stepwise conjugation of positively and negatively charged macromolecules on the surface of graphene sheets. The prominence of zwitterionic species on the surface of graphene-based 2D materials could lessen the occurrence of non-specific interactions between graphene sheets and biological systems; likewise, bacterial interactions with zwitterionic systems can be mediated to some extent through their isoelectric point (PI).[61]

Consequently, we conducted the current study where $Ti_3C_2T_x$ MXene and FG, and MXene and FG were hybridized together in three different compositions of 25% FG–75% $Ti_3C_2T_x$, 50% FG–50% $Ti_3C_2T_x$, and 75% FG–25% $Ti_3C_2T_x$, and their antibacterial activities were assessed against MRSA, and *E. coli* K1.

The synthesis of these nanomaterials and nanocomposites was followed by characterization methods which showed high purity for all the materials. SEM methods showed results for $Ti_3C_2T_x$ which matched previous literature.[36] FG was prepared to make the pristine graphene hydrophilic, and the process of functionalization resulted in pristine monolayers of FG nanosheets. The nanocomposites of FG–$Ti_3C_2T_x$ have shown fine intercalation of graphene monolayers between layers of multilayered $Ti_3C_2T_x$. The zeta potential results showed evidence of colloidal stability of synthesized nanomaterials and nanocomposites. HRTEM results showed the atomic lattice of our synthesized nanomaterials and nanocomposites, and this corroborates previous literature for $Ti_3C_2T_x$ MXene and graphene.[6,60] However, the 50% FG:50% $Ti_3C_2T_x$, 75% FG:25% $Ti_3C_2T_x$ and 25% FG:75% $Ti_3C_2T_x$ nanocomposites are novel creations of this paper and the HRTEM for these compositions as well as hydroxyl and carboxyl group functionalized graphene has been displayed.

There is good homogeneity within the MXene–functionalized graphene nanocomposite framework as SEM results show fine intercalation of FG sheets between layers of MXene sheets whilst TEM results show a fine dispersion of MXene crystals/flakes amongst a "bed" of transparent functionalized graphene sheet which has crumpled areas too. These observations lead us to infer that good harmonization has taken place within the nanocomposite framework to relay novel morphological properties to the nanocomposites. Thus, if stopped at this point, one can extrapolate that in a biological setting against microbial species, these morphological changes of the materials would come into play. In our findings, we see that the nanocomposites with composition of 50% functionalized graphene:50% $Ti_3C_2T_x$ MXene, as well as 75% functionalized graphene:25% $Ti_3C_2T_x$ MXene have much greater antibacterial activity against more resistant Gram-negative *E. coli* at higher concentration of 200 μg mL^{-1} as opposed to individual $Ti_3C_2T_x$ MXene and functionalized graphene. We postulate the reasoning for these observations to be that the homogenization of graphene within the MXene layers allows for a greater number of edge sites of both graphene and MXene to be displayed, thus increasing the chances of coming into contact with bacterial cells, creating much higher probability of these nanocomposites to kill bacteria. The parameters used in the synthesis protocol led us to the point where we successfully acquired $Ti_3C_2T_x$ MXene–functionalized graphene in three different compositions of 25% FG:75% $Ti_3C_2T_x$, 50% FG:50% $Ti_3C_2T_x$, 75% FG:25% $Ti_3C_2T_x$. Graphene in its inherent nature is hydrophobic. Therefore, we had to hydrophilize graphene in order to produce a stable colloid of graphene with deionized water (D_1 H_2O) as the base fluid. This was done by the acid treatment, and subsequent functionalization of pristine graphene with hydrophilic moieties which gave our graphene a hydrophilic nature and thus, this functionalized graphene became a stable colloid, as reflected in Table 2 where functionalized graphene has a zeta potential of −20.6 mV making it the most stable colloid, further allowing graphene to be harmonized with $Ti_3C_2T_x$ MXene to create stable colloids of 25% FG:75% $Ti_3C_2T_x$, 50% FG:50% $Ti_3C_2T_x$, 75% FG:25% $Ti_3C_2T_x$. Our EDX results show *via* the elemental composition a direct effect of the synthesis protocol whereby an increase in the weight percentage of $Ti_3C_2T_x$ MXene in the nanocomposite lead to an increase of titanium percentage whereas an increase in the weight percentage of functionalized graphene in the nanocomposite lead to an increase of carbon percentage. Thus, our synthesis parameters have had a direct effect on the pristineness, character, and activity of all the synthesized nanomaterials.

The antibacterial activity results corroborate previous papers where it was found that Gram positive bacteria are much more vulnerable to certain nanomaterials than Gram negative bacteria.[48] The reasoning for this is that the single 20–80 nm peptidoglycan layer of Gram-positive MRSA is much more prone to attack from $Ti_3C_2T_x$ MXene, and FG as well as $Ti_3C_2T_x$–FG nanocomposites, in comparison to *E. coli* K1 which has

a thinner double peptidoglycan layer of about 7–8 nm which is covered by an outer lipid membrane.[44] This is reflected in our bactericidal assay results, whereby it is shown that application of F-graphene 75% $Ti_3C_2T_x$ 25%, F-graphene 50% $Ti_3C_2T_x$ 50%, and pure F-graphene propagates complete killing of MRSA populations at concentrations of 100 and 200 μg mL^{-1}. In *E. coli* K1, the bactericidal effect is still significant but less so. For both populations of MRSA and *E. coli* K1, the nanocomposites of F-graphene 75%–$Ti_3C_2T_x$ 25%, and F-graphene 50%–$Ti_3C_2T_x$ 50% outperform pure nanomaterials of $Ti_3C_2T_x$ and FG. The findings in the bactericidal assay results are further reinforced by SEM performed with bacteria, and bacterial presence in the same vicinity as 2D nanomaterials caused interaction between bacteria and our $Ti_3C_2T_x$ MXene and functionalized graphene-based materials. Furthermore, the ROS assessment is somewhat in congruence with our bactericidal assay findings as it extrapolates that our nanomaterials and nanocomposites do lead to manifestation of oxidative stress to a large extent. As ROS is a chemical mechanism of destruction of microbial cells, we can confidently say that in this front, the nanocomposites only outperform pure functionalized graphene in generating ROS but do not surpass pure $Ti_3C_2T_x$ MXene in this regard. Thus, $Ti_3C_2T_x$ MXene reigns supreme in chemical means of bacterial cell destruction. However, the nanocomposites of $Ti_3C_2T_x$ MXene:FG (with equal or more weight percentage of FG) have overall greater cidal activity as compared to both $Ti_3C_2T_x$ MXene and FG individual counterparts and the reasoning for this can be attributed to superior physical means of bacterial cell destruction due to structural enhancements/reinforcements upon formation of nanocomposites. Thus, this superior physical activity combined with already innate good ROS activity causes the nanocomposites of 50% FG:50% $Ti_3C_2T_x$, 75% FG:25% $Ti_3C_2T_x$, to possess overall greater antibacterial potential than pure $Ti_3C_2T_x$ MXene and functionalized graphene. Our cytotoxicity results also showed that with the increase of time, the cytotoxicity of our materials increase *in vitro*. All these factors motivate further research as it shows that the $Ti_3C_2T_x$–FG nanocomposites, with more weight% of FG or equal weight% of FG and $Ti_3C_2T_x$ display more antimicrobial activity than the individual components in the composites.

Conclusion

Against MRSA bacteria, all the materials showed greater than 95% bactericidal activity at 200 μg mL^{-1} concentration, whilst against *E. coli*, at 200 μg mL^{-1}, the usage of the MXene–functionalized graphene nanocomposites completely killed bacteria, whilst individual MXene and functionalized graphene did not. This suggests that the MXene–functionalized graphene nanocomposites possessed superior antibacterial activity in comparison to the individual comprising nanomaterials. The mode of bacterial killing by these materials is shown to be a combinational of physical (direct contact) and chemical (oxidative stress) mechanisms. The finding that $Ti_3C_2T_x$–FG nanocomposites' antibacterial activity exceed that of the individual comprising $Ti_3C_2T_x$, and FG nanomaterials point to future utilities of these types of nanocomposite materials in biomedical applications.

Ethics approval

This article does not contain any studies with human participants or animals performed by any of the authors.

Author contributions

AA, SR conceived, designed, and supervised the experiments. MSS performed the experiments. MSS and NA analyzed data. MSS and JGH wrote the paper. All authors read and approved the final manuscript.

Conflicts of interest

There are no conflicts to declare.

Acknowledgements

We thank Sunway University for financial support for this research.

References

1 S. L. Percival, P. G. Bowler and D. Russell, *J. Hosp. Infect.*, 2005, **60**, 1–7.
2 S. Silver, L. T. Phung and G. Silver, *J. Ind. Microbiol. Biotechnol.*, 2006, **33**, 627–634.
3 Y. Liu, J. Yu, D. Guo, Z. Li and Y. Su, *J. Alloys Compd.*, 2019, **815**, 152403.
4 A. A. Alswat, M. B. Ahmad, M. Z. Hussein, N. A. Ibrahim and T. A. Saleh, *J. Mater. Sci. Technol.*, 2017, **33**, 889–896.
5 E. Kotb, A. A. Ahmed, T. A. Saleh, A. M. Ajeebi, M. S. Al-Gharsan and N. F. Aldahmash, *Biotechnol. Prog.*, 2020, **36**, e2907.
6 K. Rasool, M. Helal, A. Ali, C. E. Ren, Y. Gogotsi and K. A. Mahmoud, *ACS Nano*, 2016, **10**, 3674–3684.
7 A. Arabi Shamsabadi, Gh. M. Sharifian, B. Anasori and M. Soroush, *Chem. Eng.*, 2018, **6**, 16586–16596.
8 T. A. Saleh, *Environ. Technol. Innovation*, 2021, **24**, 101821.
9 J. D. Mangadlao, C. M. Santos, M. J. L. Felipe, A. C. C. De Leon, D. F. Rodigues and R. C. Advincula, *Chem. Commun.*, 2012, **51**, 2886–2889.
10 Y. Liu, Y. Zhao, B. Sun and C. Chen, *Acc. Chem. Res.*, 2012, **46**, 702–713.
11 W. J. Xu, K. Yao and K. Z. Xu, *Nanoscale*, 2019, **11**, 8680–8691.
12 W. Wang, G. Li, D. Xia, T. An, H. Zhao and P. K. Wong, *Environ. Sci.: Nano*, 2013, **4**, 782–799.
13 C. Mao, Y. Xiang, X. Liu, X. Cui, X. Yang, Z. Li, S. Zhu, Y. Zheng, K. W. Yeung and S. Wu, *ACS Nano*, 2018, **12**, 1747–1759.
14 X. Yang, J. Yang, L. Wang, B. Ran, Y. Jia, L. Zhang, G. Yang, H. Shao and X. Jiang, *ACS Nano*, 2017, **11**, 5737–5745.
15 W. Zhang, Z. Mou, Y. Wang, Y. Chen, E. Yang, F. Guo, D. Sun and W. Wang, *Mater. Sci. Eng.*, 2019, **97**, 486–497.

16 L. S. Wang, A. Gupta and M. V. Rotello, *ACS Infect. Dis.*, 2016, **2**, 3–4.
17 N. Beyth, Y. Houri-Haddad, A. Domb, W. Khan and R. Hazan, *Evid.-Based Complementary Altern. Med.*, 2015, **2015**, 246012.
18 H. A. Hemeg, *Int. J. Nanomed.*, 2017, **12**, 8211–8225.
19 H. Lin, Y. Chen and J. Shi, *Adv. Sci.*, 2018, **5**, 1800518.
20 R. Zhou and H. Gao, *Wiley Interdiscip. Rev.: Nanomed. Nanobiotechnology*, 2014, **6**, 452–474.
21 K. Yang, Y. Li, X. Tan, R. Peng and Z. Liu, *Small*, 2012, **9**, 1492–1503.
22 S. Szunerits and R. Boukherroub, *J. Mater. Chem. B.*, 2016, **4**, 6892–6912.
23 P. Kumar, P. Huo, R. Zhang and B. Liu, *Nanomaterials*, 2019, **9**, 737.
24 T. Kuila, *Biosens. Bioelectron.*, 2011, **26**, 4637–4648.
25 M. Xu, T. Liang, M. Shi and H. Chen, *Chem. Rev.*, 2013, **113**, 3766–3798.
26 X. Sun, Z. Liu, K. Welsher, J. T. Robinson, A. Goodwin, S. Zaric and H. Dai, *Nano Res.*, 2008, **1**, 203–212.
27 Z. Liu, *J. Am. Chem. Soc.*, 2008, **130**, 10876–10877.
28 V. Georgakalis, *Chem. Rev.*, 2012, **112**, 6156–6214.
29 K. Rasool, K. A. Mahmoud, D. J. Johnson, M. Helal, G. R. Berdiyorov and Y. Gogotsi, *Sci. Rep.*, 2017, **7**, 1598.
30 K. Tan, *Nanoscale*, 2018, **10**, 9525–9537.
31 I. Rago, *Antimicrobial Activity of Graphene Nanoplatelets Against Streptococcus Mutans. 15th IEEE-NANO*, 2015, pp. 9–12.
32 A. S. Abdelrazik, *Sol. Energy*, 2020, **204**, 32–47.
33 A. Anwar, R. Siddiqui, M. R. Shah and N. A. Khan, *Antimicrob. Agents Chemother.*, 2018, **62**, e00630-18.
34 P. Kumar, A. Nagarajan and D. P. Uchil, *Cold Spring Harb. Protoc.*, 2018, **6**, 095497.
35 A. Hoh and K. Maier, Comparative cytotoxicity test with human keratinocytes, HaCaT cells, and skin fibroblasts to investigate skin-irritating substances, in *Cells and Tissue Culture Models in Dermatological Res*, ed. A. Bernd, J. Bereiter-Hahn, F. Hevert and H. Holzmann, Springer, Berlin, Heidelberg, 1993, pp. 341–347.
36 N. Aslfattahi, *J. Energy Storage*, 2020, **27**, 101115.
37 L. Das, K. Habib, R. Saidur, N. Aslfattahi, S. M. Yahya and F. Rubbi, *Nanomaterials*, 2020, **10**, 1372.
38 Y. Li, X. Zhou, J. Wang, Q. Deng, M. Li, S. Du, Y. H. Han, J. Lee and Q. Huang, *RSC Adv.*, 2017, **7**, 24698–24708.
39 E. Joseph and G. Singhvi, in *Nanomaterials for Drug Delivery and Therapy*, 2019, pp. 91–116.
40 G. W. Lu and P. Gao, Emulsions and Microemulsions for Topical and Transdermal Drug Delivery, in *Handbook of Non-Invasive Drug Delivery Systems*, William Andrew Publishing, 2010, pp. 59–94.
41 R. Kumar, Lipid-based nanoparticles for drug-delivery systems, in *Nanocarriers Drug Deliv*, ed. S. Mohapatra, S. Ranjan, N. Dasgupta, R. K. Mishra and S. Thomas, Elsevier, 2019, pp. 249–284.
42 A. Lipatov, *Adv. Electron. Mater.*, 2016, **2**(12), 1600255.
43 B. Ahmed, *Nanoscale*, 2014, **8**, 7580–7587.
44 L. Ding, *Nat. Commun.*, 2018, **9**, 155.
45 W. Sarsam, A. Amiri, M. N. Zubir, H. Yarmand, S. N. Kazi and A. Badarudin, *Colloids Surf., A*, 2016, **500**, 17–31.
46 H. Yarmand, S. Gharehkhani, S. F. Shirazi, M. Goodarzi, A. Sarsam, A. Amiri, W. S. Sarsam, M. S. Alehashem, M. Dahari and S. N. Kazi, *Int. Commun. Heat Mass Transfer*, 2016, **77**, 15–21.
47 S. Ayyaru and Y. H. Ahn, *J. Membr. Sci.*, 2016, **525**, 210–219.
48 F. Alimohammadi, G. H. M. Sharifian, N. W. Attanayake, A. C. Thenuwara, Y. Gogotsi, B. Anasori and D. R. Strongin, *Langmuir*, 2018, **34**, 7192–7200.
49 L. Mei, *Theranostics*, 2019, **10**, 757–781.
50 M. Derakhshi, S. Daemi, P. Shahini, A. Habibzadeh, E. Mostafavi and A. A. Ashkarran, *J. Funct. Biomater.*, 2022, **13**, 22.
51 M. Naguib, M. Kurtoglu, V. Presser, J. Lu, J. Niu, M. Heon, L. Hultman, Y. Gogotsi and M. W. Barsoum, *Adv. Mater.*, 2011, **23**, 4248–4253.
52 L. E. Vivanco-Benavides, C. L. Martínez-González, C. Mercado-Zúñiga and C. Torres-Torres, *Comput. Mater. Sci.*, 2022, **201**, 110939.
53 M. Jukic and U. Bren, *Front. Pharmacol.*, 2022, **13**, 864412.
54 L. Daukiya, J. Seibel and S. De Feyter, *Adv. Phys.: X*, 2019, **4**, 1625723.
55 C. Murugan, V. Sharma, R. K. Murugan, G. Malaimegu and A. Sundaramurthy, *J. Controlled Release*, 2019, **299**, 1–20.
56 A. M. Jastrzebska, *J. Mater. Eng. Perform.*, 2017, **28**, 1272–1277.
57 M. F. Gholami, D. Lauster, K. Ludwig, J. Storm, B. Ziem, N. Severin, C. Böttcher, J. P. Rabe, A. Herrmann, M. Adeli and R. Haag, *Adv. Funct. Mater.*, 2017, **27**, 1606477.
58 Q. Zhenhui, P. Bharate, C. H. Lai, B. Ziem, C. Bottehers, A. Schulz, F. Beckert, B. Hatting, R. Mulhaupt, P. H. Seerberger and R. Haag, *Nano Lett.*, 2015, **15**, 6051–6057.
59 X. Xie, C. Mao, X. Liu, Y. Zhang, Z. Cui, X. Yang, K. W. K. Yeung, H. Pan, P. K. Chu and S. Wu, *ACS Appl. Mater. Interfaces*, 2017, **9**, 26417–26428.
60 L. Zhao, Y. H. Xu, T. Akasaka, S. Abe, N. Komatsu, F. Watari and X. Chen, *Biomaterials*, 2014, **35**, 5393–5406.
61 J. Park and M. Yan, *Acc. Chem. Res.*, 2013, **46**, 181–189.